ADVANCED QUANTUM TECHNOLOGIES
www.advquantumtech.com

Broadband Spectroscopy and Interferometry with Undetected Photons at Strong Parametric Amplification

Kazuki Hashimoto, Dmitri B. Horoshko, and Maria V. Chekhova*

Nonlinear interferometry with entangled photons allows for characterizing a sample without detecting the photons interacting with it. This method enables highly sensitive optical sensing in the wavelength regions where efficient detectors are still under development. Recently, nonlinear interferometry has been applied to interferometric measurement techniques with broadband light sources, such as Fourier-transform infrared spectroscopy and infrared optical coherence tomography. However, they have been demonstrated with photon pairs produced through spontaneous parametric down-conversion (SPDC) at a low parametric gain, where the average number of photons per mode is much smaller than one. The regime of high-gain SPDC offers several important advantages, such as the amplification of light after its interaction with the sample and a large number of photons per mode at the interferometer output. This work presents broadband spectroscopy and high-resolution optical coherence tomography with undetected photons generated via high-gain SPDC in an aperiodically poled lithium niobate crystal. To prove the principle, reflective Fourier-transform near-infrared spectroscopy with a spectral bandwidth of 17 THz and optical coherence tomography with an axial resolution of 11 µm are demonstrated.

1. Introduction

Spectroscopy and interferometry with broadband light sources—e.g., Fourier-transform spectroscopy (FTS)[1] and optical coherence tomography (OCT)[2,3]—are widely used in a variety of fields, such as chemistry, biology, medicine, and industry. They noninvasively measure broadband absorption/reflection spectra or high-resolution depth profiles of samples under study, exploiting the linear interference of a broadband light source, typically created by a Michelson interferometer. For FTS and OCT, the mid-infrared (MIR) region is important because it allows for measuring fundamental vibrational modes of molecules[1] and larger depths of samples with less influence from the dispersion and scattering,[4] respectively. However, infrared measurements often suffer from low measurement sensitivity because infrared detectors tend to have higher noise and lower efficiency than visible ones. Up-conversion spectroscopy[5–9] or OCT[10,11] has recently been developed to improve the sensitivity of infrared measurements by exploiting wavelength conversion processes, such as sum-frequency generation (SFG) and difference-frequency generation (DFG). In addition, electro-optic (EO) sampling[12,13] techniques have been applied to broadband infrared spectroscopy. However, those methods often require high-power MIR pulsed laser sources (e.g., fs MIR ultrashort pulsed lasers), dispersion compensation schemes, and/or other W-level lasers for wavelength conversion, which adds complexity to the system.

A quantum SU(1,1) interferometer[14,15] with a narrowband pump source enables sensitive infrared measurements with a much simpler setup. It replaces the beamsplitters of a classical interferometer with nonlinear media, such as $\chi^{(2)}$ nonlinear crystals or photonic crystal fibers, to exploit pairs of entangled photons (signal and idler) generated via spontaneous parametric down-conversion (SPDC) or spontaneous four-wave mixing (SFWM), respectively. Since the phase delays of all three photons (the pump, signal, and idler) in the interferometer contribute to the signal interferences at the output,[15] we can analyze the idler absorption or reflection of a sample without directly detecting the idler photons but by detecting the signal photons. This "measurement with undetected photons" can be applied to broadband infrared spectroscopy or OCT. Several groups have already performed spectroscopy[16–24] and OCT[25–27] with undetected photons using an SU(1,1) interferometer (or a conventional scheme of "induced coherence") based on frequency non-degenerate broadband photon pairs generated via SPDC pumped with a continuous-wave (CW) laser. Those techniques are demonstrated in the low-gain regime, where the number of photons per

K. Hashimoto, M. V. Chekhova
Max Planck Institute for the Science of Light
Staudtstr. 2, 91058 Erlangen, Germany
E-mail: kazuki.hashimoto@mpl.mpg.de
D. B. Horoshko
Univ. Lille, CNRS, UMR 8523 - PhLAM - Physique des Lasers Atomes et Molécules
Lille F-59000, France
M. V. Chekhova
Friedrich-Alexander Universität Erlangen-Nürnberg
Staudtstr. 7/B2, 91058 Erlangen, Germany

The ORCID identification number(s) for the author(s) of this article can be found under https://doi.org/10.1002/qute.202300299

DOI: 10.1002/qute.202300299

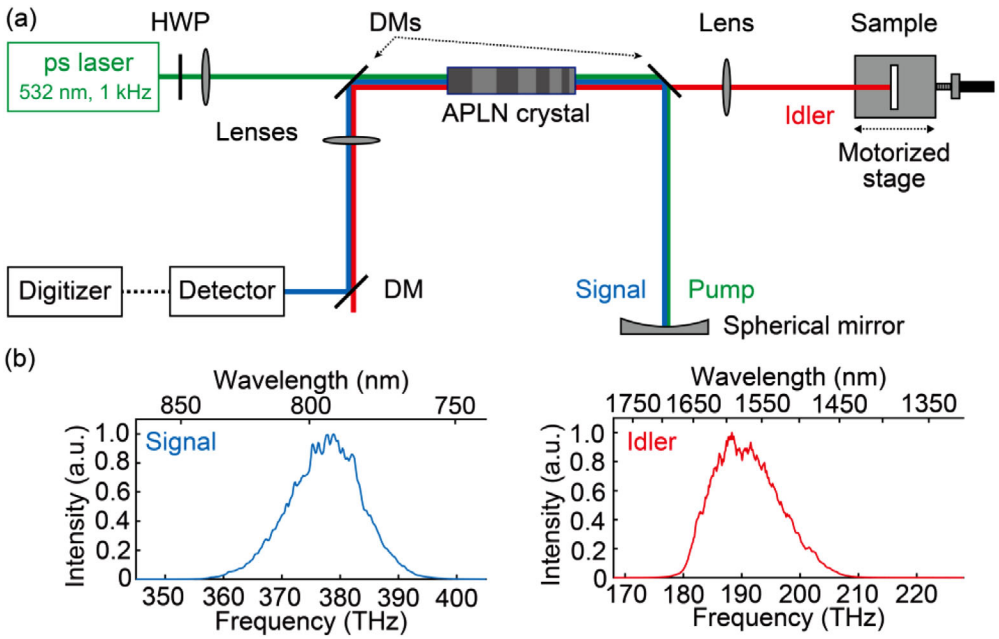

Figure 1. a) Schematic of a high-gain SU(1,1) interferometer with an APLN crystal. HWP: half-wave plate, DM: dichroic mirror. b) Broadband twin beams generated from an APLN crystal via nondegenerate SPDC pumped by a 532-nm picosecond pulsed laser.

mode generated by SPDC is much smaller than one, and the average power to be detected is up to ≈100 nW.[24]

Alternatively, SU(1,1) interferometry can be performed in the high-gain regime of SPDC with an intense pulsed pump source.[28] In the high-gain regime, the number of photons per mode is much larger than one because photon pairs, initially generated via SPDC, seed photon pair generation further along the crystal—that is, they undergo optical parametric amplification (OPA). The average power of the generated bright twin beams can be μW- or mW-level,[28] easily detected with detectors with moderate sensitivity (e.g., a Si power meter). In addition, the seeding effect allows for noninvasively interrogating a sample with a weak idler beam and detecting it as an amplified signal beam with sufficient power for detection. Machado et al.[29,30] recently performed OCT with undetected photons with an SU(1,1) interferometer operating in the high-gain regime. However, the spectral bandwidth was limited to a few THz, which resulted in the OCT depth resolution of ≈30 μm (an optical path-length difference (OPD) of ≈60 μm).

In this study, we develop an SU(1,1) interferometer based on broadband bright twin beams generated from an aperiodically poled lithium niobate (APLN) crystal[31–33] strongly pumped by a 532-nm picosecond pulsed laser. The spectral bandwidth of the twin beams generated from the APLN crystal is about three times larger than in the previous high-gain experiment.[29] We use the interferometer to demonstrate broadband FTS and high-resolution OCT with undetected photons. This method exploits the seeding effect of signal and idler photons inside the crystal, leading to an average detected power of up to ≈10 μW. As a proof-of-principle demonstration, we measure near-infrared (NIR) reflection spectra of an optical filter at a spectral bandwidth of 17 THz and OCT depth profiles of thin samples with an axial resolution of 11 μm.

2. Results

Figure 1a shows the schematic of an SU(1,1) interferometer with an APLN crystal pumped by picosecond pulses. The crystal has a poling period varying in a nonlinear fashion; see Note S1 (Supporting Information) for details. The 1-mW 532-nm picosecond laser with a repetition rate of 1 kHz is focused onto an APLN crystal to generate broadband twin beams via high-gain SPDC. After passing through the crystal, the pump and generated signal beams go to the reference arm and travel back by the same path after being reflected from a spherical mirror. The idler beam is steered into the sample arm, collimated with a lens, and reflected by a reflective sample. The pump, signal, and idler beams are combined and again focused onto the APLN crystal. The signal beam is amplified or de-amplified by the APLN crystal depending on the relative phase of the pump with respect to the sum of the signal and idler phases. The amount of amplification depends on the amplitudes of the signal and idler fields. In other words, the absorption or reflection of the idler beam interrogating a sample can be detected as an intensity modulation of the signal beam (signal interferogram). The average signal power at the interferometer output is up to ≈10 μW, and the idler power on the sample, contributing to the signal interference, is tens of nW (Note S2, Supporting Information). A time-domain signal interferogram for FTS is measured with a Si power meter with motorized-stage scanning and digitized with a digitizer. A spectral interferogram for OCT is measured with a visible spectrometer with a fixed stage position. The detailed schematic for the interferometer is described in the Experimental Section.

We first characterize the broadband twin beams generated from the APLN crystal. Figure 1b shows broadband signal and idler spectra individually measured with a visible (AvaSpec-ULS3648-USB2, Avantes) and a NIR (AvaSpec-NIR512-1.7TEC,

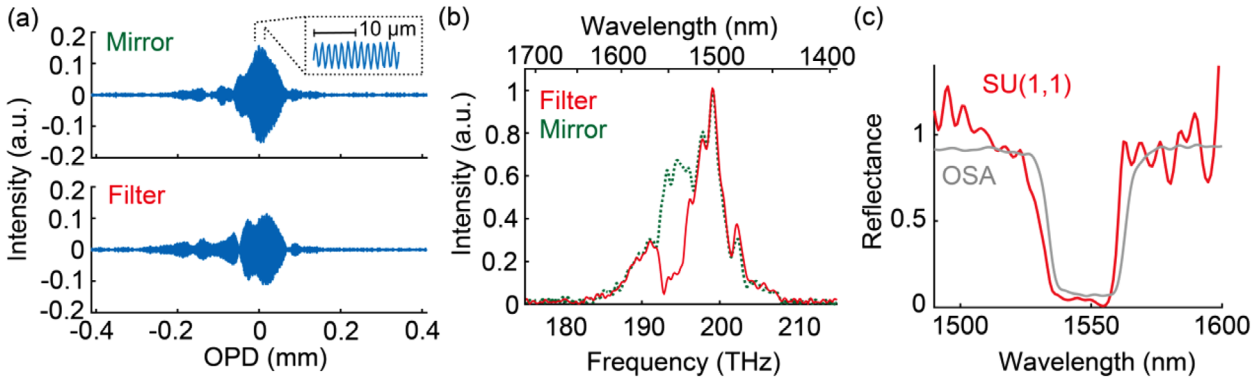

Figure 2. a) Time-domain FTS interferograms of a mirror (top) and a 1.55-μm band-pass filter (bottom) used as a sample. The inset in the upper panel shows the enlarged view of the interferogram. b) FTS reflection spectra of the mirror (dotted green) and the band-pass filter (solid red). c) Idler (intensity) reflectance spectra of the band-pass filter measured with the SU(1,1) interferometer and an OSA.

Avantes) spectrometer, respectively. We focus the radiation of a 532-nm picosecond pulsed laser with an average power of ≈350 μW onto the crystal using an f = 100 mm lens for this evaluation. The signal and idler spectra span from 768 to 824 nm (364–390 THz) and from 1470 to 1661 nm (181–204 THz) at −10-dB intensity levels, respectively. The spectral-shape difference between the twin beams is due to the wavelength-dependent sensitivity of the two spectrometers.

Next, we measure time-domain FTS interferograms and the spectra using the SU(1,1) interferometer. The FTS (signal) interferogram measured with the interferometer is described as (see Note S1, Supporting Information)

$$\Delta N\ (\tau) = \int_0^{\omega_0} I\,(\Omega)\ R_A\,(-\Omega) \cos\left[\left(\omega_0 - \Omega\right)\tau + \rho\,(\Omega)\right] \frac{d\Omega}{2\pi} \tag{1}$$

where $\Delta N(\tau)$ is the delay-dependent part of the total number of signal photons detected at the interferometer output. τ, ω_0, Ω, $R_A(-\Omega)$, and $\rho(\Omega)$ denote the idler delay, the center angular frequency of SPDC light (half of the pump angular frequency), the detuning from ω_0, the amplitude reflectance of a sample, and the phase acquired due to dispersive propagation in the crystal and sample, respectively. $I(\Omega)$ is proportional to $J\ (\Omega) = \frac{1}{2} M^4(\Omega)\sinh^2[2r(\Omega)]$, where $M(\Omega)$ and $r(\Omega)$ denote the frequency-dependent loss inside the crystal and the squeezing parameter, assuming the parametric gains of the first and second crystals are the same. Integration in Equation (1) is over the positive values of Ω corresponding to the signal band. The negative values of Ω correspond to the idler band. The phase, $\rho(\Omega)$, becomes a quadratic function due to the aperiodic poling of the crystal. The FTS spectrum is obtained by Fourier transforming Equation (1). The resultant complex spectrum is written as

$$F\ \left(\omega_0 - \Omega\right) = \frac{1}{2}\ I\,(\Omega)\ R_A\,(-\Omega)\ e^{-i\rho(\Omega)} \tag{2}$$

where Ω is limited to the signal band $[0, \omega_0]$. Equation (2) shows that the spectral intensity, $|F(\omega_0 - \Omega)|$, is linear in the amplitude reflectance, $|R_A(-\Omega)|$. The FTS interferogram and the spectrum are discussed theoretically in detail in Note S1 (Supporting Information).

The upper panel in **Figure** 2a shows an averaged FTS interferogram with radiofrequency (RF) band-pass filtering for removing higher and lower RF components outside the target RF region. The OPD of the FTS interferogram is calibrated with zero-crossing resampling with the CW interferograms of a helium–neon (HeNe) laser. We observe sinusoidal waveforms in the centerburst of the interferogram. The dotted green line in Figure 2b presents the FTS spectrum obtained by Fourier transforming the interferogram shown in the upper panel in Figure 2a. The bandwidth of the spectrum evaluated at −10-dB intensity level is 17 THz (135 nm). We also measure an FTS interferogram of a 1.55-μm optical band-pass filter used in the reflection geometry as a sample (lower panel in Figure 2a). The decay appears on one side of the interferogram because of the wavelength-dependent reflectance of the sample. The solid red line in Figure 2b shows the FTS spectrum of the 1.55-μm band-pass filter obtained by Fourier-transforming the interferogram shown in the lower panel in Figure 2a. The large dip in the spectrum originates from the passband of the band-pass filter (192 THz (1564 nm)–196 THz (1533 nm)). The (intensity) reflectance spectrum of the filter is obtained by squaring the amplitude reflectance spectrum, derived by dividing the filter spectrum by the mirror spectrum. Figure 2c shows the comparison of the reflectance spectra of the filter obtained with the SU(1,1) interferometer and an optical spectrum analyzer (OSA) (AQ6374, Yokogawa). The OSA spectra (of a mirror and a filter) are measured at 2 nm spectral resolution and convoluted with a 450-GHz-width (3.6 nm at 1550 nm) sinc function to match the instrumental spectral resolution between the two spectrometers. The slight mismatch (by ≈3 nm) of the cutoff wavelengths in the SU(1,1) interferometer case is probably because of the OPD mismatch between the idler beam and the HeNe laser for the OPD axis calibration.[1]

Next, we demonstrate spectral-domain OCT using the SU(1,1) interferometer. The OCT depth profile of the sample under study is obtained by inverse Fourier transforming the spectral interferogram. We assume the sample introduces the idler delay $\tau = 2\Delta z/c$, where $2\Delta z$ and c denote the OPD and the speed of light, respectively. The spectral interferogram is written as

$$S_{\mathrm{AC}}\ \left(\omega_0 + \Omega\right) = J\,(\Omega)\ R_A\,(-\Omega) \cos\left[\left(\omega_0 - \Omega\right)\tau + \rho\,(\Omega)\right] \tag{3}$$

The interferogram is highly chirped in frequency due to the quadratic phase, $\rho(\Omega)$, which should be compensated for

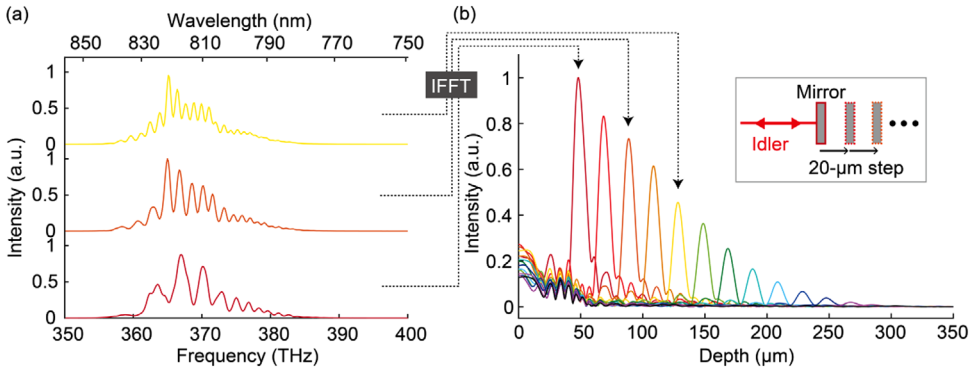

Figure 3. a) Signal spectra measured at the interferometer output with different mirror positions in the sample arm. The middle and top plots are measured at a mirror position of +40 and +80 μm from the bottom one, respectively. IFFT: inverse fast-Fourier transform. b) The depth profiles of the mirror in the sample arm for the position varied in 20-μm steps. The *X*-axis (depth) is half of the OPD between the reference and sample arms. The OCT peaks are obtained by inverse Fourier transforming the spectral interferograms after numerical processing. The sensitivity roll-off is due to the spectral resolution of the visible spectrometer. The axial resolution, determined by the peak width at 50-μm depth, is 11 μm.

numerically using the Hilbert transform before applying the inverse Fourier transform. The resultant OCT peak is described as

$$i_{\mathrm{OCT}}(z) = \left| \int_{-\infty}^{+\infty} \frac{1}{2} J(\Omega)\, R_A(-\Omega)\, e^{-i2\Omega\left(\frac{z-\Delta z}{c}\right)} \frac{d\Omega}{2\pi} \right| \tag{4}$$

where z denotes optical depth assumed to be positive. Therefore, the waveform of the OCT peak located at Δz is described as the inverse Fourier transform of $\frac{1}{2}J(\Omega)R_A(-\Omega)$, and thus, the linewidth is dominated by the bandwidth of the spectral interferogram. The spectral-domain OCT is discussed theoretically in detail in Note S1 (Supporting Information).

Figure 3a shows signal spectra measured at the interferometer output when a mirror was used as a reflective sample. The middle and top plots in the figure are obtained at a mirror (in the sample arm) position of +40 and +80 μm from the bottom one, respectively. The period of the spectral interference of the signal spectrum varies depending on the mirror position. The frequency chirp in raw interferograms is numerically corrected by exploiting the Hilbert transform before applying the inverse Fourier transform. The correction procedures are shown in the Experimental Section. Figure 3b shows the OCT depth profiles obtained by displacing the mirror in discrete 20-μm steps, with the depth shown in the *X*-axis being half of the OPD between the sample and reference arms. The peak position appropriately changes following the mirror-position changes. The axial resolution is 11 μm, which is defined by the full width at half maximum (FWHM) of the peak at a depth of 50 μm. Thus, this system can measure sub-10-μm thickness materials, accounting for the typical group index of materials (>1.3). The OCT intensity gradually decreases as its depth increases because of the visible spectrometer's spectral resolution (1.4 nm; i.e., 0.640 THz at 370 THz).

Further, we estimate the thicknesses of a lithium niobate thin film and a microscope cover glass using the SU(1,1) interferometer. **Figure** 4 shows the OCT depth profiles of the samples placed in the sample arm. The double peaks appearing in the profiles originate from the idler-beam reflections from the front and back surfaces of the samples. The amount of dispersion used for the numerical chirp compensation of the spectral interferograms is the same as in Figure 3. The intensity drop of the peak corresponding to the back face of the cover glass case is due to the sensitivity roll-off discussed in Figure 3b. The optical depths of the lithium niobate thin film and cover glass evaluated by the double-peak distances are 15 and 156 μm, respectively. Considering the group index of the samples (lithium niobate[34]: 2.2, cover glass[35]: 1.5), we estimate the thicknesses of the lithium niobate thin film and the cover glass to be 7 and 102 μm, respectively, which agree well with the reference measurements shown

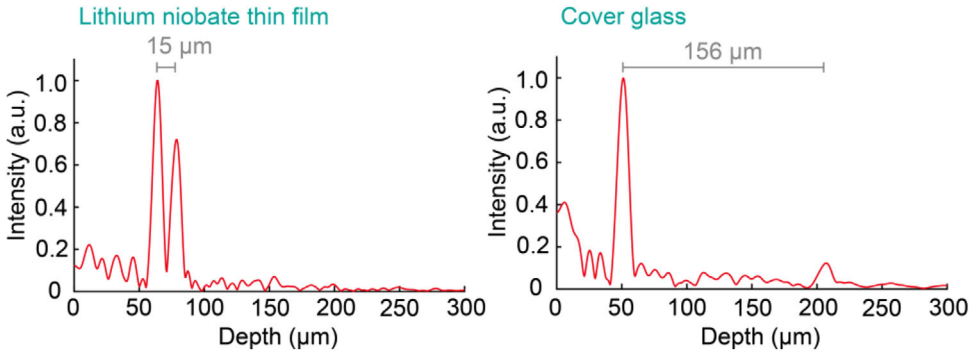

Figure 4. OCT depth profiles of a lithium niobate thin film and a cover glass. The double peaks correspond to the idler-beam reflections from the front and back surfaces of the samples.

in Note S3 (Supporting Information, 7 and 104 μm, respectively). The spectral-domain OCT for the thickness measurement of a sample is also discussed theoretically in Note S1 (Supporting Information).

3. Discussion

We evaluate the sensitivity of the developed system. The signal-to-noise ratio (SNR) for the 36-averaged FTS spectrum shown as solid-red in Figure 2b is 164, where the pump power is 1 mW, the signal power onto the photodetector is ≈5 μW, and the measurement time for a single-shot FTS interferogram is 67 s (OPD = 0.8 mm). It is obtained from the ratio of the peak intensity of the FTS spectrum to the standard deviation of the spectrum where no peaks exist. The SNR of spectral-domain OCT is estimated from the OCT depth profile in Figure 3b, where the signal power onto the spectrometer is ≈100 nW, the acquisition time is 50 ms, and the number of averages is 200. We evaluate the SNR as 46 dB following the definition of the SNR often used in OCT, which is the decibel expression of the ratio of the intensity squared to noise squared.[36] The SNR is derived from the OCT peak located at 128 μm depth as intensity and the standard deviation of the region where no peaks exist (from 166 to 239 μm) as noise.

The SNR of our system is dominated by the signal pulses' relative intensity noise (RIN), which originates from thermal statistics of the high-gain SPDC photons and the pulse-to-pulse intensity fluctuation of the pump pulses for SPDC generation. In the latter case, the amount of RIN depends on the pump power. FTS or OCT with undetected photons in the low-gain regime was performed under shot-noise-limited SNR[19,27] using highly sensitive photodetectors (e.g., avalanche photodetectors). Our method has enough signal power to be detected with moderate sensitivity photodetectors, while the RIN limits the SNR. The RIN-limited SNR remains unchanged with respect to the signal power onto the photodetector. The effect of RIN can be suppressed by increasing the number of modes and/or stabilizing the pump pulses' intensity in the future.

Compared to spectroscopy with undetected photons in the low-gain regime,[24] this method improved the average power by two orders of magnitude with a similar spectral bandwidth of ≈20 THz. Due to the use of an aperiodically poled (chirped) crystal, this method also increased the spectral bandwidth by a factor of three compared to the previously demonstrated OCT with undetected photons in the high-gain regime.[29] Our system can be improved further by modifying the setup. First, broadband twin beams can also be generated even with a periodically poled crystal by exploiting sweet spots in the group delay curve.[37] This method can be applied to hyperspectral imaging or 3D OCT using a 2D optical sensor (e.g., a charge-coupled device (CCD) or a complementary metal-oxide-semiconductor (CMOS) camera) or a 2D raster scanner. In this case, the system in the high-gain regime can use an inexpensive camera with moderate detection sensitivity because it can have a large number of photons per pixel. In addition, the measurement rate can be improved by increasing the repetition rate of the pump source (under the sufficient pump photon flux to reach the high-gain regime) and applying state-of-the-art infrared spectroscopy techniques (e.g., rapid-scan FTS[38,39] or time-stretch infrared spectroscopy[8]). Furthermore, this method can be applied to multimodal spectroscopy by exploiting a part of the pump pulses for exciting other nonlinear optical phenomena.[40]

4. Conclusion

In conclusion, we developed an SU(1,1) interferometer based on broadband bright twin beams generated from an APLN crystal strongly pumped by a pulsed light source. With this system, we performed broadband FTS spectroscopy of an optical filter in the reflection geometry at a spectral bandwidth of 17 THz and high-resolution OCT of thin transparent samples with an axial resolution of 11 μm. We also found the FTS-spectral and the OCT-peak intensity measured with a high-gain SU(1,1) interferometer were linear in the idler amplitude reflectance, while the interference visibility was nonlinear.[29] Our system allows for spectroscopy and interferometry with undetected photons at a high average detected power of up to ≈10 μW (energy per pulse: 10 nJ), which can be detected with photodetectors with moderate sensitivity. Meanwhile, the idler pulse energy on the sample (contributing to the signal interference) is expected to be tens of pJ, which is well below the typical photodamage threshold for biological samples (≈1 nJ[41] but varying for different samples and the laser parameters). Our system can be beneficial for a wide range of applications that use broadband spectroscopy and high-resolution OCT.

5. Experimental Section

SU(1,1) Interferometry: A 532-nm picosecond pulsed laser with a repetition rate of 1 kHz (PL2210A-1K-SH/TH, Ekspla) was used as a pump source for the SU(1,1) interferometer. The coherence length of the pump laser evaluated by measuring the linear interferogram was 15 ps. The average pump power was ≈1 mW (pulse energy of ≈1 μJ), and the pump polarization was adjusted with an HWP. The pump beam was focused onto a 5-mm-length type-0 APLN crystal (Gooch & Housego) using an f = 200 mm lens. The poling period of the APLN crystal varied from 7.35 to 8.76 μm along the crystal. The grating vector (defined by $2\pi/\Lambda$, where Λ denotes the poling period) varied along the crystal as the squared hyperbolic function as described in previous works.[32,33] The high-gain SPDC process inside the crystal, pumped by the 532-nm pulsed laser, generated broadband bright twin beams (signal: ≈0.8 μm, idler: ≈1.6 μm). The phase-matching bandwidth expected from the poling period variation was ≈70 THz,[31] while the experimentally measured bandwidth was up to ≈30 THz at −10-dB intensity level. The pump, signal, and idler beams were spatially and spectrally separated with a DM with a cutoff wavelength of 980 nm. The pump and signal beams went to the reference arm and traveled back to the same path after being reflected by an f = 100 mm spherical mirror. The idler beam went to the sample arm and was collimated with an f = 100 mm achromatic lens. The collimated idler beam was reflected back with a reflective sample and traveled back to the same path. The sample holder was placed on a motorized stage for scanning the OPD between the reference and sample arms. The three beams were again focused onto the APLN crystal. The signal beam at the crystal output was reflected by a DM with a cutoff wavelength of 650 nm, collimated with an f = 100-mm lens, and detected with a detector. A 550-nm long-pass filter and another DM (HR: 600–900 nm, HT: 1300–2200 nm) were installed in the signal beam path to filter out the pump and idler beams.

Detection: The time-domain FTS interferogram was detected with a Si power meter (S130VC, Thorlabs) with RF 15 Hz low-pass filtering and digitized with an 8-bit digitizer (USB-5133, National Instruments) with a sampling rate of 1.53×10^3 samples s^{-1}. The interferogram was recorded by moving the motorized stage in the sample arm with a scan velocity

of 6 µm s^{-1}. The maximum OPD of the interferogram was 0.8 mm, corresponding to the stage displacement of 0.4 mm. The OPD of the interferogram was calibrated with a simultaneously measured HeNe interferogram. The HeNe interferogram was measured with a conventional Michelson interferometer whose scanning mirror is on the same motorized stage as the SU(1,1) interferometer. For the spectral-domain OCT measurements, the signal beam was coupled into a 400-µm-core multimode fiber and detected with a visible grating-based spectrometer (AvaSpec-ULS3648-USB2, Avantes) with a spectral resolution of 1.4 nm (0.640 THz at 370 THz). The power coupled into the multimode fiber was attenuated with neutral density filters. The spectral interferogram was measured at a fixed motorized-stage position.

Data Analysis: The FTS and the HeNe interferograms were numerically RF band-pass filtered. The filtered FTS interferogram was resampled at the zero-crossing points of the HeNe interferogram. The corrected FTS interferogram was coherently averaged, zero-filled, and Fourier transformed to obtain the FTS (idler) spectrum. For OCT, the measured signal spectrum was divided by the background spectrum measured at a sufficiently large OPD, whose fringes were not resolvable with the visible spectrometer. The DC offset of the resultant interferogram was numerically subtracted. The dispersion appearing in the interferogram (mainly due to the aperiodic poling of the APLN crystal) was numerically corrected by extracting the complex waveform with the Hilbert transform and adding a group delay dispersion of −3500 fs^2 to the spectral phase.[27,42] The corrected spectral interferogram was triangular-apodized, zero-filled, and inverse Fourier transformed to obtain the OCT depth profile.

Supporting Information

Supporting Information is available from the Wiley Online Library or from the author.

Acknowledgements

K.H. acknowledges the financial support by JSPS (Overseas Research Fellowships). D.B.H. acknowledges the support of Agence Nationale de la Recherche (France) via grant ANR-19-QUAN-0001 and of Franco-Bavarian University Cooperation Center via grant FK-09-2023. M.V.C. acknowledges the support by QuantERA II Programme (project SPARQL) that has received funding from the European Union's Horizon 2020 research and innovation programme under Grant Agreement No 101017733, with the funding organization Deutsche Forschungsgemeinschaft.

Open access funding enabled and organized by Projekt DEAL.

Conflict of Interest

The authors declare no conflict of interest.

Data Availability Statement

The data that support the findings of this study are available from the corresponding author upon reasonable request.

Keywords

Fourier-transform spectroscopy, high parametric gain, nonlinear interferometry, optical coherence tomography, undetected photons

Received: September 11, 2023
Revised: November 14, 2023
Published online:

[1] P. R. Griffiths, J. A. De Haseth, *Fourier Transform Infrared Spectrometry*, John Wiley & Sons, Hoboken, **2006**.
[2] D. Huang, E. A. Swanson, C. P. Lin, J. S. Schuman, W. G. Stinson, W. Chang, M. R. Hee, T. Flotte, K. Gregory, C. A. Puliafito, J. G. Fujimoto, *Science* **1991**, *254*, 1178.
[3] T. Dresel, G. Häusler, H. Venzke, *Appl. Opt.* **1992**, *31*, 919.
[4] C. S. Colley, J. C. Hebden, D. T. Delpy, A. D. Cambrey, R. A. Brown, E. A. Zibik, W. H. Ng, L. R. Wilson, J. W. Cockburn, *Rev. Sci. Instrum.* **2007**, *78*, 123108.
[5] T. A. Johnson, S. A. Diddams, *Appl. Phys. B* **2012**, *107*, 31.
[6] T. W. Neely, L. Nugent-Glandorf, F. Adler, S. A. Diddams, *Opt. Lett.* **2012**, *37*, 4332.
[7] Z. Chen, T. W. Hänsch, N. Picqué, *arXiv:2003.06930* **2020**.
[8] K. Hashimoto, T. Nakamura, T. Kageyama, V. R. Badarla, H. Shimada, R. Horisaki, T. Ideguchi, *Light Sci Appl* **2023**, *12*, 48.
[9] M. Liu, R. M. Gray, L. Costa, C. R. Markus, A. Roy, A. Marandi, *Nat. Commun.* **2023**, *14*, 1044.
[10] N. M. Israelsen, C. R. Petersen, A. Barh, D. Jain, M. Jensen, G. Hannesschläger, P. Tidemand-Lichtenberg, C. Pedersen, A. Podoleanu, O. Bang, *Light Sci Appl* **2019**, *8*, 11.
[11] N. M. Israelsen, P. J. Rodrigo, C. R. Petersen, G. Woyessa, R. E. Hansen, P. Tidemand-Lichtenberg, C. Pedersen, O. Bang, *Opt. Lett.* **2021**, *46*, 4558.
[12] A. S. Kowligy, H. Timmers, A. J. Lind, U. Elu, F. C. Cruz, P. G. Schunemann, J. Biegert, S. A. Diddams, *Sci. Adv.* **2019**, *5*, eaaw8794.
[13] I. Pupeza, M. Huber, M. Trubetskov, W. Schweinberger, S. A. Hussain, C. Hofer, K. Fritsch, M. Poetzlberger, L. Vamos, E. Fill, T. Amotchkina, K. V. Kepesidis, A. Apolonski, N. Karpowicz, V. Pervak, O. Pronin, F. Fleischmann, A. Azzeer, M. Zigman, F. Krausz, *Nature* **2020**, *577*, 52.
[14] B. Yurke, S. L. Mccall, J. R. Klauder, *Phys. Rev. A* **1986**, *33*, 4033.
[15] M. V. Chekhova, Z. Y. Ou, *Adv. Opt. Photonics* **2016**, *8*, 104.
[16] D. A. Kalashnikov, A. V. Paterova, S. P. Kulik, L. A. Krivitsky, *Nat. Photonics* **2016**, *10*, 98.
[17] A. V. Paterova, S. M. Maniam, H. Yang, G. Grenci, L. A. Krivitsky, *Sci. Adv.* **2020**, *6*, eabd0460.
[18] C. Lindner, S. Wolf, J. Kiessling, F. Kühnemann, *Opt. Express* **2020**, *28*, 4426.
[19] C. Lindner, J. Kunz, S. J. Herr, S. Wolf, J. Kießling, F. Kühnemann, *Opt. Express* **2021**, *29*, 4035.
[20] Y. Mukai, M. Arahata, T. Tashima, R. Okamoto, S. Takeuchi, *Phys. Rev. Appl.* **2021**, *15*, 034019.
[21] A. V. Paterova, Z. S. D. Toa, H. Yang, L. A. Krivitsky, *ACS Photonics* **2022**, *9*, 2151.
[22] Y. Mukai, R. Okamoto, S. Takeuchi, *Opt. Express* **2022**, *30*, 22624.
[23] P. Kaufmann, H. M. Chrzanowski, A. Vanselow, S. Ramelow, *Opt. Express* **2022**, *30*, 5926.
[24] C. Lindner, J. Kunz, S. J. Herr, J. Kießling, S. Wolf, F. Kühnemann, *APL Photonics* **2023**, *8*, 051301.
[25] A. V. Paterova, H. Yang, C. An, D. A. Kalashnikov, L. A. Krivitsky, *Quantum Sci Technol* **2018**, *3*, 025008.
[26] A. Vallés, G. Jiménez, L. J. Salazar-Serrano, J. P. Torres, *Phys. Rev. A* **2018**, *97*, 023824.
[27] A. Vanselow, P. Kaufmann, I. Zorin, B. Heise, H. M. Chrzanowski, S. Ramelow, *Optica* **2020**, *7*, 1729.
[28] T. Sh. Iskhakov, A. M. Pérez, K. Yu. Spasibko, M. V. Chekhova, G. Leuchs, *Opt. Lett.* **2012**, *37*, 1919.
[29] G. J. Machado, G. Frascella, J. P. Torres, M. V. Chekhova, *Appl. Phys. Lett.* **2020**, *117*, 094002.
[30] A. Rojas-Santana, G. J. Machado, M. V. Chekhova, D. Lopez-Mago, J. P. Torres, *Phys. Rev. A* **2022**, *106*, 033702.
[31] D. B. Horoshko, M. I. Kolobov, *Phys. Rev. A* **2017**, *95*, 033837.

[32] M. V. Chekhova, S. Germanskiy, D. B. Horoshko, G. K.. Kitaeva, M. I. Kolobov, G. Leuchs, C. R. Phillips, P. A. Prudkovskii, *Opt. Lett.* **2018**, *43*, 375.
[33] D. B. Horoshko, M. I. Kolobov, F. Gumpert, I. Shand, F. König, M. V. Chekhova, *J. Mod. Opt.* **2020**, *67*, 41.
[34] Optical constants of LiNbO3 (Lithium niobate), Zelmon et al. 1997: n(e) 0.4–5.0 µm, https://refractiveindex.info/?shelf=main&book=LiNbO3&page=Zelmon-e (accessed: December 2023).
[35] Optical constants of SCHOTT – multiple purpose, D 263® T eco Thin Glass, https://refractiveindex.info/?shelf=glass&book=SCHOTT-multipurpose&page=D263TECO (accessed: December 2023).
[36] W. Drexler, J. G. Fujimoto, *Optical Coherence Tomography*, Springer International Publishing, Berlin, Germany, **2015**.
[37] A. Vanselow, P. Kaufmann, H. M. Chrzanowski, S. Ramelow, *Opt. Lett.* **2019**, *44*, 4638.
[38] K. Hashimoto, T. Ideguchi, *Nat. Commun.* **2018**, *9*, 4448.
[39] K. Hashimoto, M. Takahashi, T. Ideguchi, K. Goda, *Sci. Rep.* **2016**, *6*, 21036.
[40] F. Sinjab, K. Hashimoto, V. R. Badarla, J. Omachi, T. Ideguchi, *Opt. Express* **2020**, *28*, 20794.
[41] V. V. Yakovlev, *J. Raman Spectrosc.* **2003**, *34*, 957.
[42] M. Wojtkowski, V. J. Srinivasan, T. H. Ko, J. G. Fujimoto, A. Kowalczyk, J. S. Duker, *Opt. Express* **2004**, *12*, 2404.